ORIGINAL PAPER

The impacts of Mn ion incorporation on the structural, optical, and magnetic properties of hematite NPs

S. James Jayaseelan[1] · K. Parasuraman[1] · D. Benny Anburaj[2] · M. Jothibas[3] · B. Arunkumar[4]

Abstract

The research focuses on the study of the ferromagnetic behaviour of α-Fe_2O_3 NPs. Iron nanoparticles show prominent ferromagnetic behaviour compared with other metal oxide nanoparticles. Regarding technical applications, doping can be employed to increase the ferromagnetic properties of α-Fe_2O_3 NPs. The effect of Mn at various weight percentages on α-Fe_2O_3 produced by the sol–gel technique was investigated. The XRD data of pure and Mn-doped α-Fe_2O_3 results corroborated the rhombohedral crystal structure. The FT-IR results were in agreement with the XRD data. From the SEM images, the synthesized nanoparticles show spherical symmetry. From the UV–visible studies, an optical band gap of the synthesized sample is approximately 1.93–1.83 eV. The bandgap varies with the value varying depending on the amount of doped material in the sample. The VSM tests revealed that α-Fe_2O_3 with 3 wt% of Mn doping exhibits a slight hard-ferromagnetic behaviour than others.

Keywords Sol–gel · Hematite · Nanoparticles · Magnetic property · Optical properties

Introduction

The α-Fe_2O_3 synthesis finds numerous applications, including magnetic materials, data storage devices, biomedicine, catalysts, and toxic waste remediation [1, 2]. However, its magnetic behaviour is very high on comparing with other applications. We are currently developing new nanopowder fabrication methods and optimizing existing ones. It can be used to control the size and morphology of nanoparticles using a low-cost one-pot synthesis. In comparison, sol-gel fabrication is the most versatile, requiring only a small amount of a low-cost precursor and a simple synthesis procedure. Hematite is the most common of the four phases. α-Fe_2O_3 has weak ferromagnetism below 950K. An α-Fe_2O_3 has a cubic spinel structure when heated below 49K and below the temperature 49 °C, which it becomes to be an orthorhombic crystalline structure. Magnetic nanoparticles developed in magnetic structures are one of the most effective methods with the added benefit of controlling particle size, shape, and morphology. The superparamagnetic transition in magnetic nanocomposite devices limits their stability in electrical and high-density data storage systems [3–6]. Because nanoparticle interactions can increase media noise, high-density recording requires grain isolation to reduce dipolar contacts. Hematite nanoparticles made by various chemical processes have strong dipolar interactions [7–9]. The chemical coating of nanoparticles by nonmagnetic particles reduced their interactions [10]. Mn-doped iron oxide nanoparticles, hematite, and a sol-gel method were used to investigate the magnetic characteristics of α-Fe_2O_3 nanoparticles. Nanoparticle interactions were investigated using the system's dynamic properties. To determine the degree of interaction between magnetic moments of particles, we employed the Arrhenius and Vogel–Fulcher equations, as well as the frequency-sensitive parameter.

✉ S. James Jayaseelan
  jamesjayaseelanphd@gmail.com

1 Department of Physics, Poompukar College – Autonomous (Affiliated to Bharathidasan University, Tiruchirappalli), Melaiyur, Tamil Nadu, India

2 Dharmapuram Gnanambigai, Government Arts College for Women (Affiliated to Bharathidasan University, Tiruchirappalli), Mayiladuthurai, Tamil Nadu, India

3 PG and Research Department of Physics, T.B.M.L. College (Affiliated to Bharathidasan University, Tiruchirappalli), Porayar, Tamil Nadu, India

4 Sir Issac Newton College of Engineering and Technology (Affiliated to Anna University – Chennai), Nagapattinam, Tamil Nadu, India

Researchers are continually looking for new materials with superior qualities in order to meet future societal demands and improve technological innovation. The possibility of combining these oxides in composite structures to produce multifunctional materials has recently rekindled interest in perovskites (Fe_2O_3) and spinels (Fe_2O_4). Composite powders made of perovskites and spinels are commonly used [11–13]. Nanoscale composites are gaining popularity as a way to create materials with unique or better features. Solar cells with high efficiency, fuel cells with high efficiency, catalysis, capacitors with high efficiency, superconductors with high efficiency, electrochemical sensing, underwater devices, spintronics device design, and other technologies have all been shown [14–16]. They retain multiferroic, thermoelectric, dielectric, optical, and other properties [17]. Many properties of Mn-doped iron oxide ($Mn–Fe_2O_3$) have piqued the interest of engineers and technologists. Both the sol-gel and hydrothermal techniques [18, 19] use the widely available manganese chloride sputtering targets. Microwave and wireless communication applications utilize the Mn-doped α-Fe_2O_3 material because of their exceptional and promising dielectric properties. Ferrites are electrically, magnetically, and dielectrically distinct magnetic ceramics. Due to their remarkable electromagnetic capabilities, spinel ferrites, with the chemical formula Mn-doped α-Fe_2O_3, are the most extensively utilised magnetic materials in the industry [20, 21]. Spinel ferrites have the chemical formula $Mn–Fe_2O_3$. Spinel ferrites have high electrical resistivity, low eddy current and dielectric loss, high saturation magnetization, high permeability, good chemical stability, ease of preparation, and low fabrication cost [22]. These properties make manganese ferrite ($MnFe_2O_4$) nanoparticles ideal for high-density information storage devices, biomedical nanotechnology, and medicine applications [23]. The unusual mechanical, electrical, optical, and magnetic properties of submicron and nanoscale materials and composites have attracted recent research [24–26]. The mechanical and electrical properties of nanoceramic materials with nano-size crystallites are superior to those of bulk-grained materials. Multiferroic composite materials are made by combining ferrite and ferroelectric ceramics. Many scientific and technological applications rely on magnetoelectric materials. Most synthesis procedures used to make nanoparticles face considerable challenges due to the coarseness and aggregation of nanocrystals at higher temperatures. To solve these challenges, nanoparticles have been dispersed in matrix-like materials such as silica, glass, resin, and polymers [27–31]. There are several promising physical methods, including electron beam evaporation, sputtering techniques, pulsed laser deposition, and several chemical ways of synthesizing methods, such as hydrothermal, co-precipitation, electrochemical, sol-gel technique, and so forth, which are deemed to be experiencing quite an inconvenience. Sol-gel-based nanoparticle synthesis is a well-established method for producing high-quality α-Fe_2O_3 hematite nanomaterials. This allows it more flexibility to modify its shape, size, and morphology depending on the application. Using a sol-gel method has several advantages. It is of low cost as it has precise composition, purity, and molecular homogeneity control. This study describes the cost-effective sol-gel synthesis of α-Fe_2O_3 nanoparticles. The nanoparticles are then characterized for their structural, optical, and magnetic properties using X-ray diffraction, scanning electron microscopy with EDAX, ultraviolet spectroscopy, Fourier transforms infrared (FT-IR), and vibrating sample magnetometer (VSM).

Experimental procedure

The α-Fe_2O_3 nanoparticles were synthesized by using iron chloride dihydrate as the precursor and ammonia solution as the reducing agent. The reaction was performed in an 100 mL of aqueous medium at a room temperature. The 99.98% purity of iron chloride di-hydrate ($FeCl_3 \cdot 2H_2O$) and 1 wt% manganese chloride dehydrate ($MnCl_2 \cdot 2H_2O$) solution was made up in a beaker with constant magnetic stirring. 20 mL ammonia solution was added drop wisely into the mixture solution. The solution mixture was consistently stirred at 80 °C, and a gelatinous formation of brown colour precipitation appeared suddenly, which is schematically represented in Fig. 1. The final precipitate was filtered and washed thoroughly for many turns in demineralized water before even being dried in a drying hot air oven at 100 °C for 20 h and calcinated at 500 °C for 5 h. α-Fe_2O_3 nanoparticles have been synthesized using a similar approach for 3 wt% and 5 wt.%, accordingly. Figure 2 depicts the step-by-step experimental procedure flow chart.

Characterization techniques

The crystal structure and phase of synthesized α-Fe_2O_3 nanoparticles were characterized by X-ray diffraction analysis via the (SHIMADZU-XRD 6000) characterization instrument. The morphology of the α-Fe_2O_3 nanoparticles was analysed by scanning electron microscopy (Hitachi S-4500 SEM instrument). The absorption spectra were measured using a UV–Vis spectrophotometer (SHIMADZU-UV 1800). PL study was carried out at room temperature using a VARIAN spectrophotometer equipped with a 450 W Xenon lamp as the excitation source. Fourier transform infrared (FT-IR) spectra were recorded in the range 4000–500 cm^{-1} using a BRUKER: RFS 27. The magnetic measurement was carried out in a
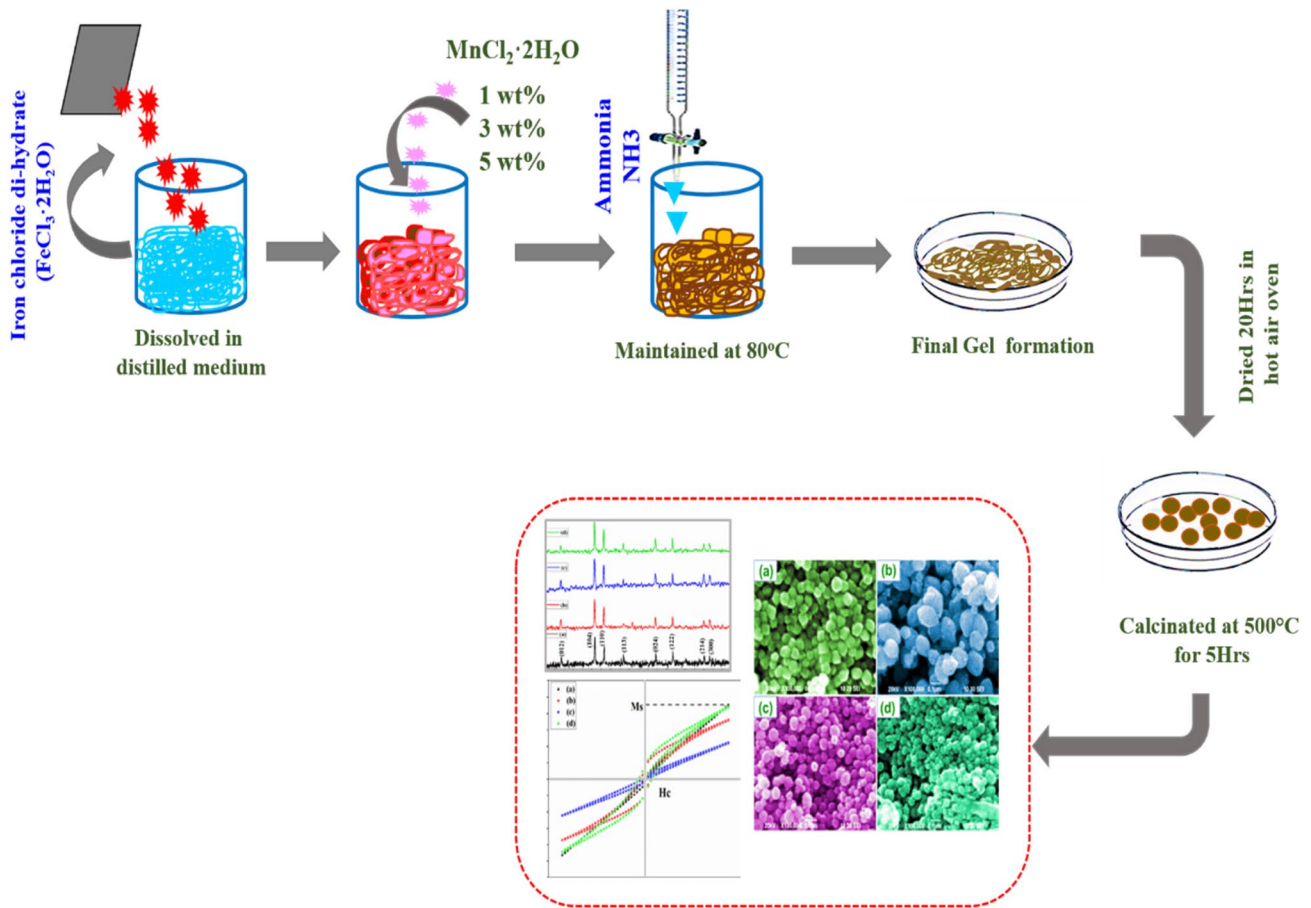
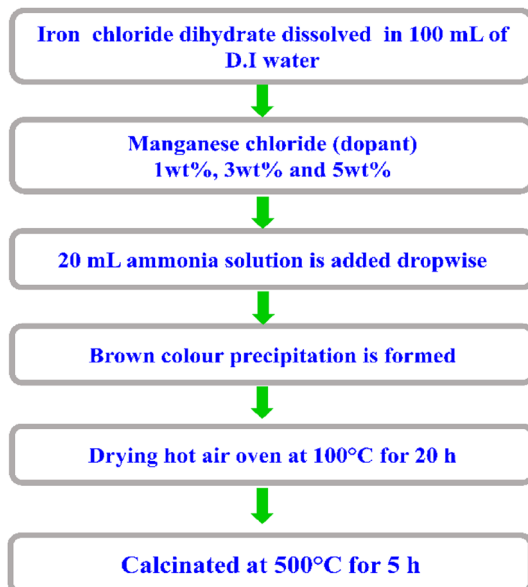**Fig. 1** Schematic diagram of the experimental procedure

Fig. 2 Flowchart of the experimental procedure

vibrating sample magnetometer (lakeshore VSM 7140) at room temperature.

Results and discussion

Structural analysis

In order to analyse the crystalline property and its dopant effects on crystal, symmetry causes adequate examination through the XRD characterization at different doping weight percentages. Figure 3a–d depicts the structure of pure and 1 wt%, 3 wt% and 5 wt% of Mn-doped α-Fe_2O_3 NPs, having a good agreement with rhombohedral structure matched with JCPDS card No. 89-1165. The diffraction planes (012), (104), (110), (113), (024), (116), (122), (214) and (300) corresponding to diffraction angles 24.1°, 33.1°, 40.8°, 84°, 64.9° and 64°, respectively. No other impurity peak was noticed in the XRD spectra. The diffraction peak intensity has significantly increased with increasing dopant percentage at 1 wt%, 3 wt%, and 5 wt%, which attributes to the crystallinity of nanoparticles
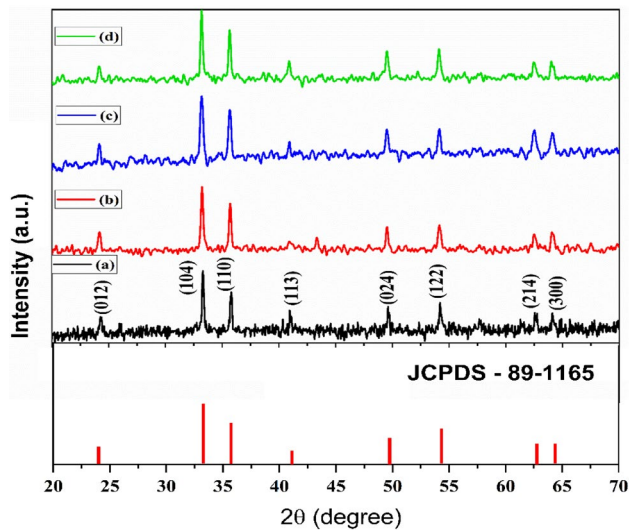
Fig. 3 a–d XRD spectra for pure and 1 wt%, 3 wt% and 5 wt% of Mn doped α-Fe$_2$O$_3$ nanoparticles

Table 1 Structural parameters of pure and 1 wt%, 3 wt% and 5 wt% of Mn-doped Fe$_2$O$_3$

NPs sample names	Crystallite size (nm)—D	Dislocation density × 10^{15} (l/m^2)	Microstrain (ε)
Pure α-Fe$_2$O$_3$	25	1.567	0.00143
1 wt% α-Fe$_2$O$_3$	29	1.128	0.00121
3 wt% α-Fe$_2$O$_3$	22	1.982	0.00161
5 wt% α-Fe$_2$O$_3$	15	4.014	0.00229

[32–41]. Moreover, the crystal size is evaluated using the following Scherrer equation;

$$D = k\lambda / \beta \cos \theta \qquad (1)$$

where D is the crystallite size, k is the Scherrer coefficient (0.89), λ is the wavelength of the X-ray (0.15418 nm, Cu-kα, β is the full width at half maximum (FWHM), and θ is the diffraction angle [42]. The estimated crystallite sizes of pure and Mn-doped iron oxide having the average crystallite sizes were decreased subsequently. The broadness of the diffraction peak influences crystal size and the internal lattice strain. Different concentrations 5 wt% increasing the wt% concentration above 5 wt% results in similar Mn-doped α-Fe$_2$O$_3$ rhombohedral phase with a reduction in the size of the Mn-doped α-Fe$_2$O$_3$ NPs, because the heat treatment 500 °C to involves changes in crystallite size and stabilizes a more face centred rhombohedral structure according to the size effect. The grain size increases at 1 wt% of Mn and then decreases with an increase in the dopant concentration 3 wt% and 5 wt%). This behaviour was expected because the heating facilitates the diffusion and agglomeration of the particles. The diffraction peaks become more intense, and it can be attributed to the thermally promoted crystallite growth. Calcinated temperature clearly promotes grain growth with a further increase in wt% of concentration (5 wt%). The surface-to-volume ratio, and thus the fraction of surface atoms in nanoparticles, increases as the particle size is reduced. This can improve the surface reaction of the nanoparticles [43]. During annealing under an oxygen atmosphere, grain size increase will cause crystallite size effects and promotes. The calculated lattice constant values

are less than the standard value, which strongly indicates stress in the nanoparticles. The lattice defects like δ and $\mathcal{E}$ have shown a decreasing trend with increasing Mn-doped percentages, which may be due to the improvement of crystallinity and the high orientation along (104) plane orientation. In comparison with pure, crystallite size and structural parameters were increased for the doped. The decrement of crystallite size of α-Fe$_2$O$_3$ nanoparticles 29–22 nm is reported when weight percentage increases from 1 to 3 wt% [44]. Similarly, a decrease in crystallite size of α-Fe$_2$O$_3$, nanoparticles from 22 to 15 nm is reported when weight percentage increases to 5 wt% [45, 46]. The dislocation density and microstrain were evaluated by using the following relation [47, 48].

$$\delta = 1/D^2 \qquad (2)$$

$$\varepsilon = \beta \cos \theta / 4 \qquad (3)$$

The dislocation density and microstrain for nanoparticles have increased from 1.128 to 4.014 lines/m^2 and 0.001216 to 0.002293 with a decrease of crystal size [49–51]. The structural parameters such as dislocation density (δ) and microstrain (ε) of pure and α-Fe$_2$O$_3$ nanoparticles are listed in Table 1.

Functional group analysis

The confirmative examination of different molecular entities integrated with synthesizing of metal-oxide NPs and, importantly, the vibrational characterization has supported the existence of α-Fe$_2$O$_3$ metal oxide bonding complexes were effectively identified by Fourier-Transform Infrared spectroscopy in an exploration range around 4000 cm^{-1} and 400 cm^{-1} at room temperature. The found FT-IR spectra of pure and various proportions of Mn ion-doped α-Fe$_2$O$_3$, treated at a similar calcination temperature, are depicted in Fig. 4a–d. From the absorption spectra, three prominent absorption bands can be found in the reported spectra, in the ranges of 3465–434 cm^{-1}. Initially, the broad absorption bands centred at 3465 and 3160 cm^{-1} correspond to the
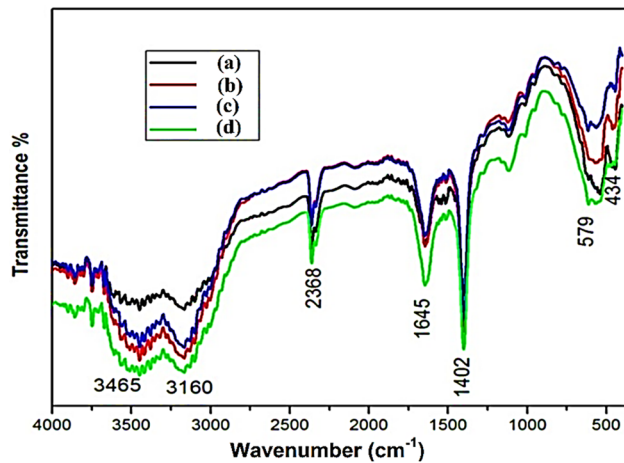
Fig. 4 **a–d** FT-IR spectra of pure and 1 wt%, 3 wt% and 5 wt% of Mn-doped α-Fe$_2$O$_3$ NPs

stretching vibrational mode O–H (hydroxyl groups and water molecules) incorporated iron oxide NPs [52]. Secondly, the band reported at 1645 and 1402 cm^{-1} has been assigned as O–H bending modes [53]. Despite the oven drying at 100 °C for several hours, the detection of –OH molecular vibration and bending modes of H–O–H molecules indicate that residues of moisture are still stable. The sharp noticeable band obtained at 517 cm^{-1} and 434 cm^{-1} was strongly corresponding to the Fe–OH stretching mode of vibration [54]. A peak of 2368 cm^{-1} has been linked to the attribution of carbon-di-oxide molecules from the environmental surroundings [55]. The 5 wt% of Mn-doped iron oxide NPs, in particular, showed sharper and stronger peaks, and their peak positions were displaced towards the higher wavelength range than the other samples, indicating that doped Mn ions effectively disrupt the host metal oxide symmetry. The observed functional vibrations are presented in Table 2.

SEM with EDAX

The modifications to the microstructural ambiance of different proportions of Mn ion dopant infused on α-Fe$_2$O$_3$ NPs have a similar method of preparation, and the temperature of calcination was appropriately characterized through the scanning electron microscope (SEM) and the microstructural status of the surface of a sample. Figure 5a–c demonstrates the different surface conditions of 1 wt%, 3 wt%, and 5 wt% of Mn-doped α-Fe$_2$O$_3$ NPs, respectively. We can see the micrographs; all the synthesized NPs were clearly exhibiting a greater number of particles having spherical and few had bulbous shaped surface morphology. Moreover, all possess homogeneous-sized particle arrangements, which is noteworthy to mention. While increasing the dopant ions percentage, the particle size was reduced exponentially with increasing agglomeration between the Nano-sized particles [56, 57]. And one thing, we related that the pure, 1 wt%, 3 wt%, and 5 wt% of Mn-doped α-Fe$_2$O$_3$ show more voids and emptiness as intermediate the nanoparticles. On the other hand, the 5wt% of NPs shows next to each other. The spherical-shaped particles are coherently oriented as a cluster of microstructures encompassing the studied surface. Notably, the α-Fe$_2$O$_3$ has doped with a 5 wt% Mn ion to confirm a strong crystallinity behaviour and a good boundary surface. Furthermore, the existence of incorporated atomic species in all the pure and Mn-doped NPs was characterized by the energy-dispersive X-ray analysis. Figure 6a–d, which is included inside that representative SEM image, shows the observed EDAX spectra and as it could only have Fe—iron atoms, Mn—manganese atoms, and O—oxygen atoms in the synthesized nanoparticles. Otherwise, no other unknown atoms were to be found in the elemental analysis, which directly attributes to the purity of the synthesized NPs. We additionally plot the histogram using ImageJ software for the particle size distribution over the synthesized scanned samples surface to express the influence of dopant ions in particles of pure α-Fe$_2$O$_3$ as depicted in SEM images. Figure 7a–d has been plotted

Table 2 Assigned functional molecular vibrations of pure and 1 wt%, 3 wt% and 5 wt% of Mn-doped α-Fe$_2$O$_3$ nanoparticles

| Assigned functional molecular groups	Pure α-Fe$_2$O$_3$	1 wt% Mn-α-Fe$_2$O$_3$	3 wt% Mn-α-Fe$_2$O$_3$	5 wt% Mn-α-Fe$_2$O$_3$	Band strength
Stretching vibrational mode O–H	3465 cm^{-1} and 3160 cm^{-1}	3467 cm^{-1} and 3162 cm^{-1}	3469 cm^{-1} and 3165 cm^{-1}	3471 cm^{-1} and 3166 cm^{-1}	Strong
Carbon-di-oxide molecules	2368 cm^{-1}	2370 cm^{-1}	23,670 cm^{-1}	2373 cm^{-1}	Medium
O–H bending modes	1645 and 1402 cm^{-1}	1648 and 1410 cm^{-1}	1651 and 1413 cm^{-1}	1652 and 1414 cm^{-1}	Strong
Fe–OH stretching mode of vibration	517 cm^{-1} and 434 cm^{-1}	519 cm^{-1} and 437 cm^{-1}	522 cm^{-1} and 438 cm^{-1}	525 cm^{-1} and 439 cm^{-1}	Strong
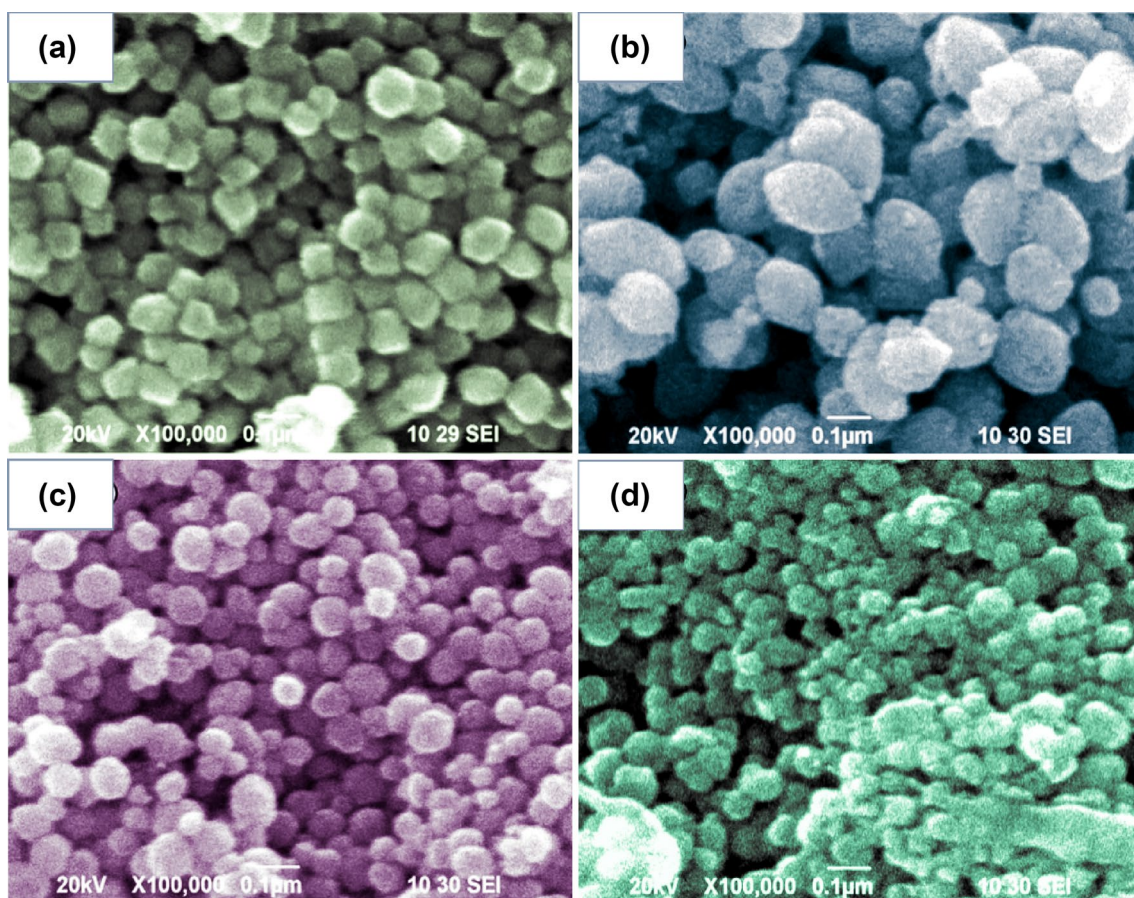
Fig. 5 **a–d** SEM micrographs of pure and 1 wt%, 3 wt% and 5 wt% of Mn doped α-Fe$_2$O$_3$ NPs

in a consistent way between particle size and the number of particles was distributed over the illuminated area. A significant number of particles sizes in pure α-Fe$_2$O$_3$ was accumulated at 31 nm, 38 nm, 27 nm, and 21 nm for all the following 1 wt%, 3 wt%, and 5 wt% Mn-doped NPs, respectively. Appropriately, all the estimated results have a good agreement with our earlier X-ray diffraction studies.

Optical analysis

In pure α-Fe$_2$O$_3$ semiconducting NPs, significant impacts of Mn ions inclusion coordinators were affecting optical phenomena as well as bandgap predominantly. As a result, the most suited UV–Visible spectroscopy analysis method can be used to study it. In addition, UV–Vis studies were characterized out over the range between 200 and 800 nm wavenumber ranges for the mentioned NPs. The absorption will arise between 200 and 400 nm, attributed to the nano-materials having some vital absorbance zones, according to the reported spectra. The observed absorption spectra of α-Fe$_2$O$_3$ NPs, which exhibit strong absorption bands there in wave number area at 239 nm, can be seen in Fig. 8a–d. The

stated absorption zone arises due to a continuous charge transport transition from O^{2-} in the 2p electronic state to Fe^{3+} in the 3d electronic transitions [58–61]. It is commonly recognized that quantum confinement processes cause a blue shift to occur in an absorption spectrum of the synthesized samples. Their Absorption spectra strength might increase at 5 wt% of Mn ion-doped α-Fe$_2$O$_3$ NPs and vary with respect to the dopant inclusion percentages, which would be an intriguing insight into the impact of different doping incorporation levels and crystallite size reduction. Additionally, with a reduction in 1–3 wt% of ultraviolet, optical intensity was decreased, which indicated a unique characteristic of the defect in the interrupted space, and the order–disorder effects of α-Fe$_2$O$_3$NPs are closely related [62]. Employing the Tauc relation, the bandgap energy— eV quantities of the synthesized NPs are true and accurate as from Spectral data in the ongoing work. The below-mentioned optical parameters are (α) for the absorption coefficient and ($h\nu$) for the photon energy, which are provided hereunder [63].
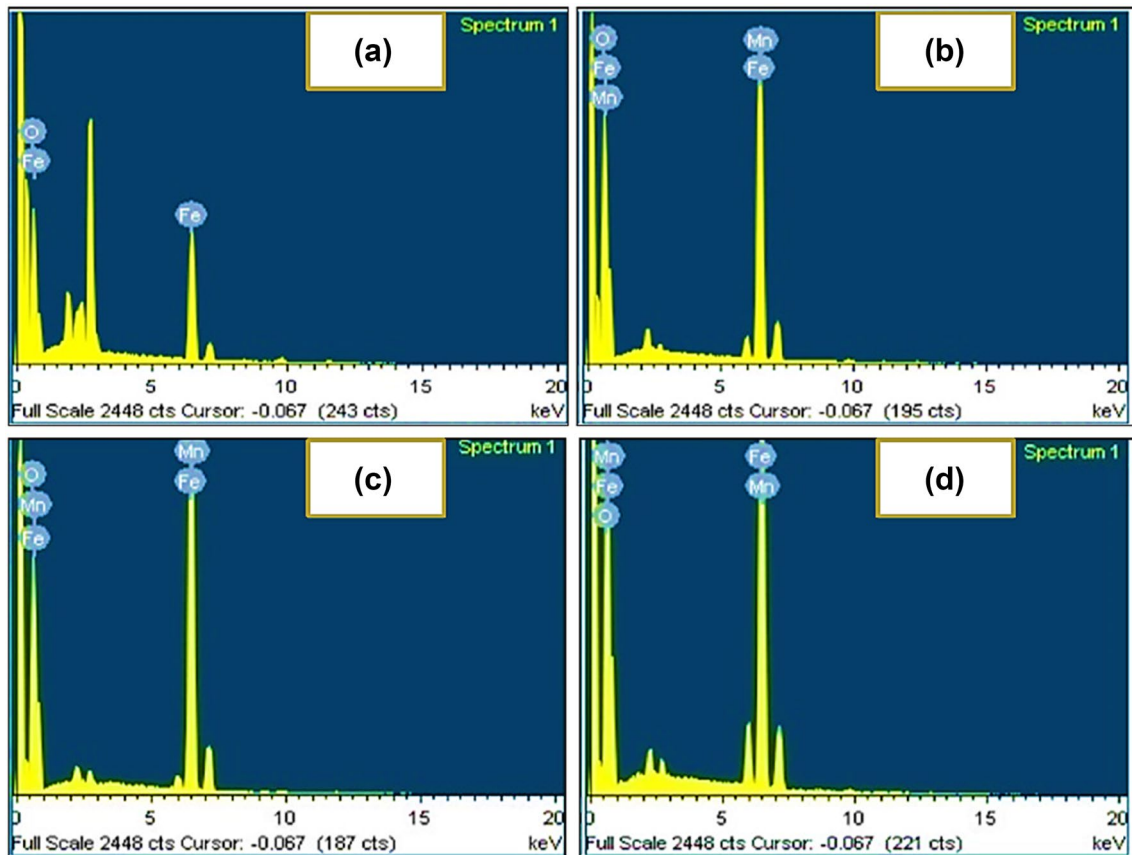
Fig. 6 **a–d** EDAX spectra of pure and 1 wt%, 3 wt% and 5 wt% of Mn doped α-Fe$_2$O$_3$ NPs

$$\alpha = \frac{2.303A}{l} \tag{4}$$

and

$$\alpha h\nu = A\left(h_\nu - E_\mathrm{g}\right)^n \tag{5}$$

Energy bandgap of synthesized semiconductor nanoparticles; the eV is denoting (Electron Volt), $n = 2$ is the allowable direct transition, and (ν) is the frequency of radiant energy. Graphically bandgap energy is plotted as the values of $(h)^2$ versus $h\nu$ plotted with the linear region via interpolation, allowing the optical energy band gap of pure and Mn-doped α-Fe$_2$O$_3$ NPs to be estimated. Extrapolating the plot by using the linear portion of the graph to intersect the $h\nu$ axis got the bandgap estimates as shown in Fig. 9a–d. Energy band gaps of Mn-doped hematite nanoparticles have been computed and determined to be 1.90, 1.85, 1.86, and 1.83 eV for (1 wt%, 3 wt% to 5 wt%) of Mn-doped α-Fe$_2$O$_3$ NPs, respectively. With increasing Mn dopant concentrations, the bandgap energy of α-Fe$_2$O$_3$ NPs tends to decrease. The above results are related to the establishment of vacant positions within-host lattice and also the introduction of

new energy levels in the iron oxide. It is possible because the interfaced dopant will release holes along the α-Fe$_2$O$_3$ top of the valence band, which will undoubtedly reduce the bandgap energy [64, 65]. Table 3 lists the bandgap values of pure and different Mn-doped α-Fe$_2$O$_3$NPs.

Magnetic properties

Through the most versatile approach of Vibrating Sample Magnetometer examination -VSM, the magnetic behaviours of the synthesized pure and different percentages of Mn ions doped α-Fe$_2$O$_3$ NPs could be studied. A consistent external applied magnetic field measuring between the (− 15,000 Oe to 15,000 Oe) was used for the essential magnetic study, in addition to the overall characterizations carried out in ambient temperature measurements, respectively. Figure 10a–d depicts the observed hysteresis curve, which was plotted by the magnetization as a factor of different external magnetic fields to different Mn concentrations 1 wt%, 3 wt%, and 5 wt%) of α-Fe$_2$O$_3$ NPs. As a result, the synthesized material magnetism outcomes were fully reliant on the degree of particle organization, morphology, and dopant influence in the host network, accordingly. Because of the sequential
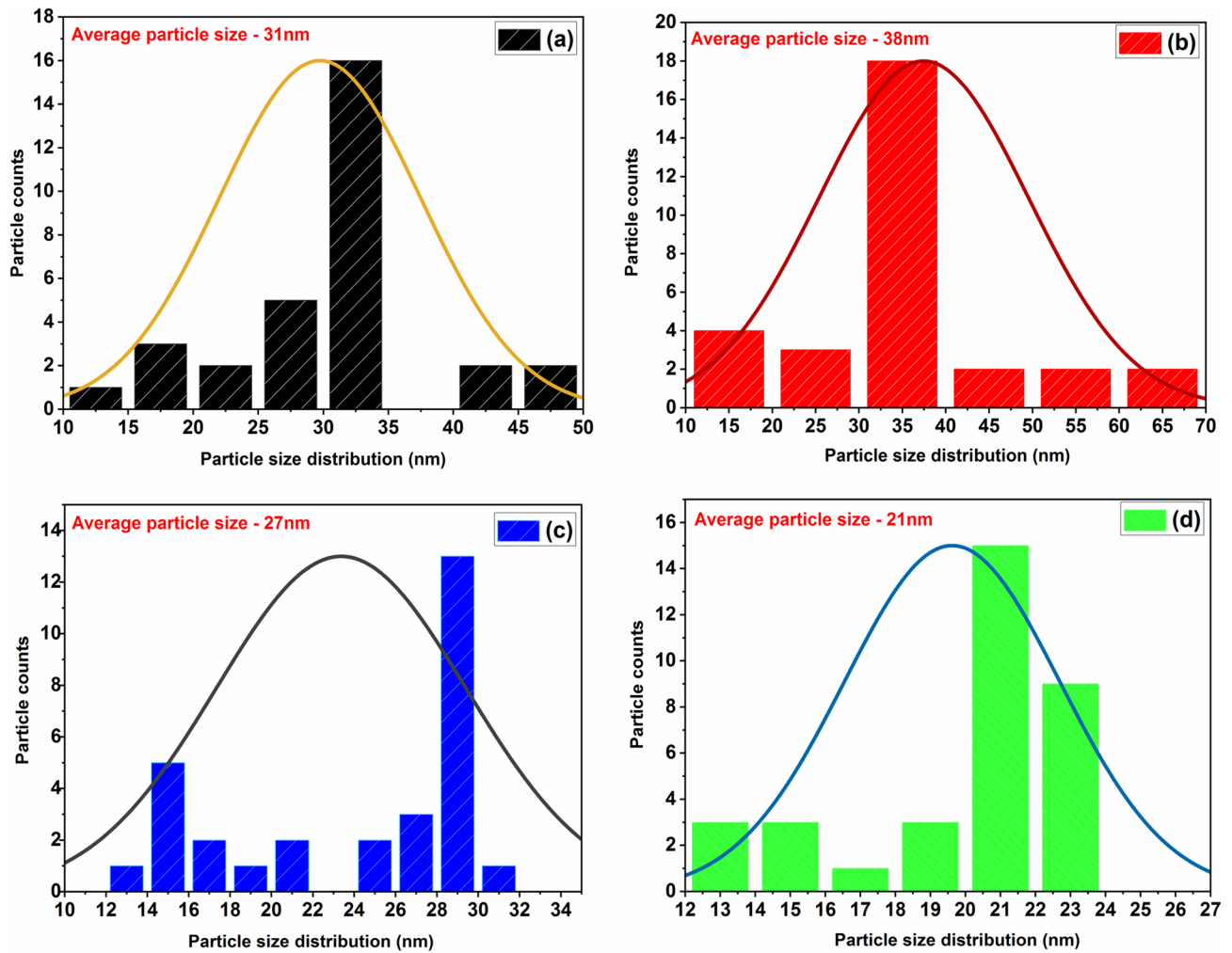
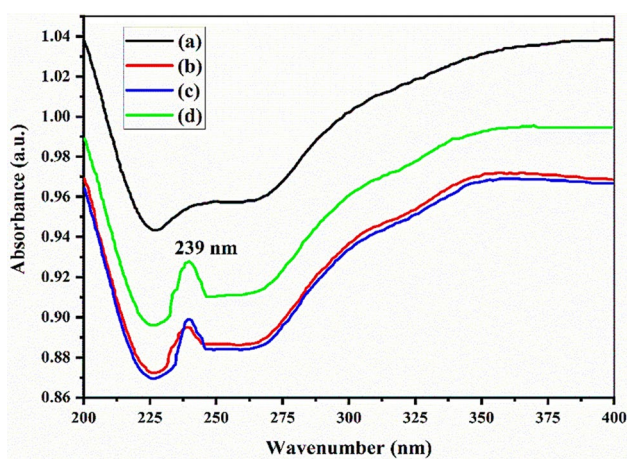**Fig. 7** **a–d** Histogram plot of pure and 1 wt%, 3 wt% and 5 wt% of Mn doped α-Fe₂O₃ NPs

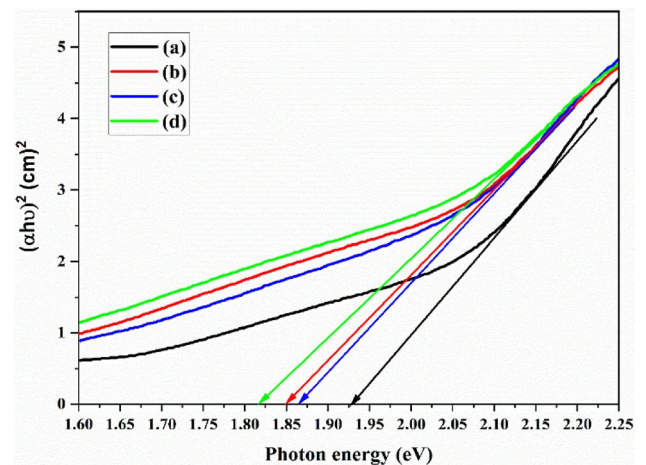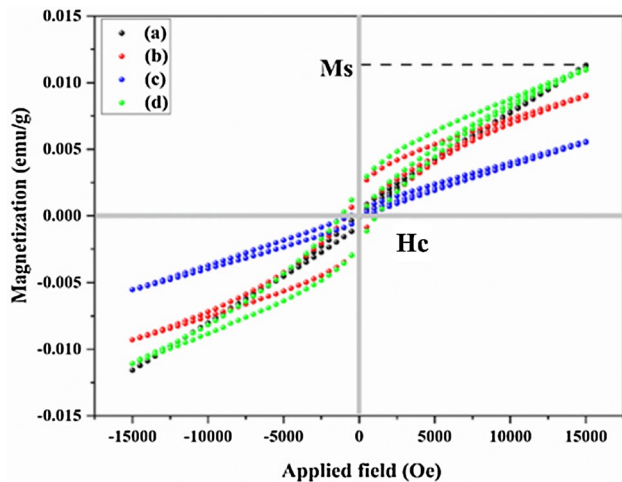**Fig. 8** **a–d** UV spectra for pure and 1 wt%, 3 wt% and 5 wt% of Mn doped α-Fe₂O₃ NPs

Fig. 9 **a–d** Optical band gap of pure and 1 wt%, 3 wt% and 5 wt% of Mn doped α-Fe₂O₃ NPs

Table 3 Calculated bandgap energies of pure and 1 wt%, 3 wt% and 5 wt% of Mn-doped α-Fe$_2$O$_3$ nanoparticles

NPs sample (wt%)	Bandgap (eV)
Pure	1.930
1 wt%	1.850
3 wt%	1.865
5 wt%	1.837

Fig. 10 a–d Hysteresis curves of undoped and 1 wt%, 3 wt% and 5 wt% of Mn-doped α-Fe$_2$O$_3$ NPs

confluences of manganese ions dopant, we investigated certain changes and implications in essential magnetic properties, including such saturation field (Ms), magnetic remanent (Mr), and magnetic coercive (Hc) that will occur in α-Fe$_2$O$_3$ NPs. The 1 and 3 wt% of Mn ion-doped α-Fe$_2$O$_3$ NPs show the maximum coercive values Hc -1092 Oe and 1879.5 Oe from 535.37 Oe of pure α-Fe$_2$O$_3$NPs. It's important to note that the pure α-Fe$_2$O$_3$NPs nanoparticles, with such a coercivity of 535.37Oe, also exhibit ferromagnetism over ambient temperature [66]. As the dopant levels of Manganese rise at 5 wt%, proportionally, the coercive field values increase to 1860.5 Oe, as shown in the figure. As a result, the higher dopant content is linked to the dopant ions preferring to site upon that iron and oxide linked matrix in a random fashion. The host transitional geometry of α-Fe$_2$O$_3$ NPs is easily disrupted by repeated dopant interfacing. Moreover, the material net dipole value of the α-Fe$_2$O$_3$ was frequently affected by this process. In conclusion, the Mn-doped α-Fe$_2$O$_3$ NPs offered interesting facts and relationships. The results that clearly mentioned factor that the magnetic coercivity depends on crystallite size. In addition, the M–H hysteresis loops of all the synthesized nanoparticles indicate ferromagnetic characteristics in terms of symmetric hysteresis and saturation magnetization. This is mostly due to the effects

of a smaller average crystal size of Mn-doped nanoparticles. Several changes in the magnetic saturation of Mn-doped samples such as 5.54 emg^{-1}, 4.62 emg^{-1}, 4.57 emg^{-1}, and 7.44 emg^{-1} are clearly lower than that of pure nanoparticles that are 74 emg^{-1} [67]. This occurrence could be accounted for by the impact of smaller crystallite size, which occurs when a non-collinear magnetic spin orientation at the surface decreases the magnetic moment of α-Fe$_2$O$_3$ NPs [68, 69]. A comparative statement here as the earlier research has expressed that coercivity and retentivity completely based on the nanostructured material size, structure, several structural influenced from the dopant and nature of the material morphology. The prior author Alex Rufus et al. has stated the Hc values with the size of nano-crystallites at 50.5 nm for coercivity at 972 Oe, 43.4 nm for coercivity at 906 Oe, and 29.6 nm for coercivity at 799 Oe, respectively [70]. Moreover, Zohra Nazir Kayani et al. the prior researcher reports that the hematite material shows coercivity at 100 Oe, and 1000 Oe at relative calcination temperatures 400 °C and 1000 °C with the same sol–gel technique only varied precursor materials. It has worth mentioning here that the present report should show the higher coercivity at 1331.2 Oe value just attained at 500 °C calcination temperature. The overall magnetization was decreased, while the Mn ions interrupts in the hematite domain locations. It may be associated with a significant number of defect sites, resulting in a magnetic moment deficiency due to a lower magnetic saturation response. The magnetization strength of the particles is proportional to the number of typical molecules per magnetic domains region, which is crucial [71]. In this study, hematite with different percentages of Mn-doped α-Fe$_2$O$_3$ results in enhanced magnetic behaviour for all the nanoparticles to be in weak ferromagnetic nature [72, 73]. Because of the high coercivity strength, the nanoparticle's waves formed as single domains. An increase in magneto-crystalline anisotropy conferred by Mn to the oxide results in an increase in coercivity up to 5 wt% for Mn ion doping [74–77]. The Mn-doped α-Fe$_2$O$_3$ NPs have been determined the optimal level trustworthy of hard magnetic applications wave based on such validated observations. Table 4 lists the determined sample magnetization, coercive field, and remanent magnetization strength measurements for all of the NPs.

Table 4 Magnetic parameters of pure and 1 wt%, 3 wt% and 5 wt% of Mn-doped α-Fe$_2$O$_3$ nanoparticles

Mn doping (wt%)	Ms (emu/g)$\times 10^{-3}$	Mr (emu/g)$\times 10^{-6}$	Hc (Oe)
Pure	5.54	332.88	535.37
1 wt%	4.62	898.08	1092
3 wt%	4.57	692.74	1879.5
5 wt%	7.44	511.19	1860.5

Conclusion

Mn-doped α-Fe$_2$O$_3$ hematite nanoparticles were produced using sol–gel synthesis. Iron oxide diffraction patterns confirm hematite's crystallinity. The average crystallite size fell from 29 to 15 nm as doping increased. As the weight percentage grew, the direct bandgap energy of α-Fe$_2$O$_3$ nanoparticles decreased. SEM pictures of Mn-doped α-Fe$_2$O$_3$ NPs showed aggregation and non-homogeneous clusters dispersion. However, 5 wt% of Mn-doped NPs were highly crystalline and well scattered over the surface area. Pure α-Fe$_2$O$_3$ NPs exhibit problematic ferromagnetic behaviour, but 5 wt% Mn ions doped α-Fe$_2$O$_3$ NPs considerably impact the parent hematite material. Dopant collapse causes host lattice homogeneity, coercivity, and retentivity. The 5 wt% Mn is an excellent doping material for α-Fe$_2$O$_3$ NPs, we found. From the results, we aimed to conduct comparable investigations with different precursor molarities and co-dopant Mn-percentages.

Declarations

Conflict of interest The authors have no relevant financial or non-financial interest to disclose.

References

1. Mimura N, Takahara I, Saito M, Hattori T, Ohkuma K, Ando M (2008) Dehydrogenation of ethylbenzene to styrene with carbon dioxide over ZrO$_2$-based composite oxide catalysts Springer Science+Business Media. LLC 45:61. https://doi.org/10.1007/s10563-007-9039-8

2. Lottici P, Baratto C, Bersani D, Antonioli G, Montenero A, Guarneri M (2012) Structural and optical characterization of sol–gel derived boron doped Fe$_2$O$_3$ nanostructured films. J. Sol Gel Sci. Technol. 62(3):397. https://doi.org/10.1007/s10971-012-2740-8

3. Liu H, Wei Y, Li P, Zhang FY, Sun Y (2007) Catalytic synthesis of nanosized hematite particles in solution. Mater Chem Phys 102:1–6. https://doi.org/10.1016/j.matchemphys.2006.10.001

4. Kadya ASA, Gabera M, Husseinb MM, Ebeid E-ZM (2011) Structural and fluorescence quenching characterization of hematite nanoparticles, Spectrochim Acta A Mol Biomol Spectrosc 83:398

5. Cannas C, Ardu A, Niznansky D, Peddis D, Piccaluga G, Musinu A (2006) Synthesis and characterization of CoFe$_2$O$_4$ nanoparticles dispersed in a silica matrix by a sol−gel autocombustion method. J Sol Gel Sci Technol 60:266. https://doi.org/10.1021/cm060650n

6. Raming TP, Winnubst AJA, van Kats CM, Philipse AP (2002) The synthesis and magnetic properties of nanosized hematite (α-Fe$_2$O$_3$) particles. J Colloid In Sci 249:346. https://doi.org/10.1006/jcis.2001.8194

7. Khirade PP, Birajdar AD, Raut A, Jadhav K (2016) Multiferroic iron doped BaTiO$_3$ nanoceramics synthesized by sol–gel auto combustion: influence of iron on physical properties. Ceram Int 42:12441. https://doi.org/10.1016/j.ceramint.2016.05.021

8. Sanpo N, Wen C, Berndt CC, Wang J (2015) Multifunctional spinel ferrite nanoparticles for biomedical applications. Adv Funct Mater 2015:183

9. Rondinelli JM, May SJ, Freeland JW (2012) Control of octahedral connectivity in perovskite oxide heterostructures: an emerging route to multifunctional materials discovery. Mater Res Soc 37:261. https://doi.org/10.1557/mrs.2012.49

10. Hull D, Clyne TW (1996) https://doi.org/10.1017/CBO9781139170130

11. Sapate D, Kale C, Pandit A, Jadhav K (2014) Structural, magnetic and magnetoelectric properties of the magnetoelectric composite material. J Mater Sci Mater Electron 25:3659. https://doi.org/10.1007/s10854-014-1938-7

12. Testino A (2006) Preparation of multiferroic composites of BaTiO$_3$–Ni$_{0.5}$Zn$_{0.5}$Fe$_2$O$_4$ ceramics. J Eur Ceram Soc 26(2006):3031–3036. https://doi.org/10.1016/j.jeurceramsoc.2006.02.022

13. Dimos D, Mueller C (1998) Perovskite thin films for high-frequency capacitor applications. Annu Rev Mater Sci 28:397. https://doi.org/10.1146/annurev.matsci.28.1.397

14. Ishihara T (2009) Universality in statistics at small scales of turbulence: a study by high resolution DNS, turbulence and interactions. Springer, Berlin. https://doi.org/10.1007/978-3-642-00262-5_3

15. Tressler JF, Howarth TR, Huang D (2006) A comparison of the underwater acoustic performance of single crystal versus piezoelectric ceramic-based "cymbal" projectors. J Acoust Soc Am 119:879. https://doi.org/10.1121/1.2150153

16. Bibes M, Barthélémy A (2008) The room-temperature manipulation of magnetization by an electric field using the multiferroic BiFeO$_3$ represents an essential step towards the magnetoelectric control of spintronics devices. Nat Mater 7:425. https://doi.org/10.1038/nmat2189

17. Galasso FS (2013) Structure, properties and preparation of perovskite-type compounds. Elsevier, New York. https://doi.org/10.1016/c2013-0-02117-2

18. Gao D, Guo R (2010) Structural and electrochemical properties of yttrium-doped barium zirconate by addition of CuO. J Alloys Compd 493:288. https://doi.org/10.1016/j.jallcom.2009.12.082

19. Khirade PP, Birajdar SD, Humbe AV, Jadhav K (2016) Structural, electrical and dielectrical property investigations of Fe-Doped BaZrO$_3$ nanoceramics. J Electron Mater 45:3227. https://doi.org/10.1007/s11664-016-4472-y

20. Sanchez LE, Mc Donald AJ (1998) Google Patents, Mountain View

21. Farooq M, Rita RA, Rossnagel SM (2001) Google Patents, Mountain View

22. Parida S, Rout SK, Cavalcante LS, Sinha E, Siu Li M, Subramanian V, Gupta N, Gupta VR, Varela JA, Longo E (2012) Structural refinement, optical and microwave dielectric properties of BaZrO$_3$. Ceram Int 38:2129. https://doi.org/10.1016/j.ceramint.2011.10.054

23. Ali WFFW, Rejab NA, Othman M, Ain MF, Ahmad ZA (2012) An investigation of dielectric resonator antenna produced from silicon (100) enhanced by strontium doped-barium zirconate films. J Solgel Sci Technol 61:411. https://doi.org/10.1007/s10971-011-2641-2

24. Mathew DS, Juang R-S (2007) An investigation of dielectric resonator antenna produced from silicon (100) enhanced by strontium doped-barium zirconate films. Chem Eng J 129:51–65. https://doi.org/10.1016/j.cej.2006.11.001

25. O'Handley RC, Huang JK, Bono DC, Simon J (2008) Improved wireless, transcutaneous power transmission for in vivo applications. IEEE Sens J 8:57–62. https://doi.org/10.1109/Jsen.2007.912899

26. Song N et al (2018) Facile synthesis and high-frequency performance of CoFe$_2$O$_4$ nanocubes with different size. J Magn Magn Mater 451:793. https://doi.org/10.1016/j.jmmm.2017.12.019

27. Vinayak V, Khirade PP, Birajdar SD, Alange R, Jadhav K (2019) Structural, microstructural and magnetic properties of sol–gel-synthesized novel BaZrO$_3$-CoFe$_2$O$_4$ nanocomposite. J Supercond Nov Magn 28:3351–3356. https://doi.org/10.1007/s40097-019-0307-8

28. Amiri S, Shokrollahi H (2013) The role of cobalt ferrite magnetic nanoparticles in medical science. Mater Sci Eng C 33:1–8. https://doi.org/10.1016/j.msec.2012.09.003

29. Ding Y (2018) Single-walled carbon nanotubes wrapped CoFe$_2$O$_4$ nanorods with enriched oxygen vacancies for efficient overall water splitting. ACS Appl Energy Mater 2:1026. https://doi.org/10.1021/acsaem.8b01338

30. Lin Y-S (2006) Multifunctional composite nanoparticles: magnetic, luminescent, and mesoporous. Chem Mater 18:5170. https://doi.org/10.1021/cm061976z

31. Kumar AS (2016) Multiferroic and magnetoelectric properties of Ba$_{0.85}$Ca$_{0.15}$Zr$_{0.1}$Ti$_{0.9}$O$_3$–CoFe$_2$O$_4$ core–shell nanocomposite. J Magn Magn Mater 418:294. https://doi.org/10.1016/j.jmmm.2016.02.065

32. Kanakadurga M, Raju P, Murthy SR (2013) Preparation and characterization of BaTiO$_3^+$MgCuZnFe$_2$O$_4$ nanocomposites. J Magn Magn Mater 341:112. https://doi.org/10.1016/j.jmmm.2013.04.037

33. Nitta A, Nakamura H, Komatsu T, Matusita K (1989) Interface reactions between silicon dioxide-lead oxide glass and manganese zinc ferrite. J Am Ceram Soc 72:1351. https://doi.org/10.1111/j.1151-2916.1989.tb07650.x

34. Paterson J, Devine R, Phelps A (1999) Complex permeability of soft magnetic ferrite/polyester resin composites at frequencies above 1 MHz. J Magn Magn Mater 196:394. https://doi.org/10.1016/S0304-8853(98)00772-0

35. Bayrakdar H (2011) Complex permittivity, complex permeability and microwave absorption properties of ferrite–paraffin polymer composites. J Magn Magn Mater 323:1882. https://doi.org/10.1016/j.jmmm.2011.02.030

36. Khirade PP, Birajdar SD, Raut A, Jadhav K (2016) Effect of Fe-substitution on phase transformation, optical, electrical and dielectrical properties of BaTiO$_3$ nanoceramics synthesized by sol-gel auto combustion method. J Electroceram 37:110. https://doi.org/10.1007/s10832-016-0044-z

37. Newnham RE, McKinstry SE, Ikawa H (1990) Multifunctional ferroic nanocomposites. Mater Res Soc Symp Proc 175:161. https://doi.org/10.1557/proc-175-161

38. Kroll E, Winnik FM, Ziolo R (1996) In situ preparation of nanocrystalline γ-Fe$_2$O$_3$ in Iron(II) cross-linked alginate gels. Chem Mater 8:1594. https://doi.org/10.1021/cm960095x

39. Ayyub P, Multani M, Barma M, Polkar VR, Vijayaraghavan RJ (1988) Phys C Solid State Phys 21:2229

40. Tronc. E, Prene. P, J. P. Jolivet. J.P, d'Orazio. F, Lucari. F, Fiorani. D, Godinho. M, et al., (1995) Magnetic behaviour of γ-Fe$_2$O$_3$ nanoparticles by M6ssbauer spectroscopy and magnetic measurements. Hyperfine Interact 95:129. https://doi.org/10.1007/BF02146310

41. Concas G, Ennas G, Gatteschi D, Musinu A, Piccaluga G, Sangregorio C, Spano G, Stanger JL, Zedda D (1998) Characterization of iron oxide nanoparticles in an Fe$_2$O$_3$–SiO$_2$ composite prepared by a sol–gel method. Chem Mater 10:495. https://doi.org/10.1021/cm970400u

42. Wang JP, Luo HL (1994) J Magn Magn Mater 131:54

43. Niznansky, Daniel ; Rehspringer, Jean Luc ; Drillon, Marc (1994) Preparation of magnetic nanoparticles (y-Fe$_2$O$_3$) in the silica matrix. IEEE Trans Magn 30:821. https://doi.org/10.1109/20.312420

44. Mirza IM, Sarfraz AK, Hasanain SK (2014) Effect of surfactant on magnetic and optical properties of α-Fe$_2$O$_3$ nanoparticles. Acta Phys Pol A 126:1280. https://doi.org/10.12693/APhysPolA.126.1280

45. Rendon JL (1981) IR spectra of powder hematite: effects of particle size and shape. Clay Miner 16:375. https://doi.org/10.1180/claymin.1981.016.4.06

46. Mansur HS, Sadahira CM, Souza AN, Mansur AAP (2008) FTIR spectroscopy characterization of poly(vinyl alcohol) hydrogel with different hydrolysis degree and chemically crosslinked with glutaraldehyde. Mater Sci Eng C 28:539. https://doi.org/10.1016/j.msec.2007.10.088

47. Bharathi S, Nataraj D, Seetha M, Mangalaraj D, Ponpandian N, Masuda Y, Senthil K, Yong K (2010) Controlled growth of single-crystalline, nanostructured dendrites and snowflakes of α-Fe$_2$O$_3$: influence of the surfactant on the morphology and investigation of morphology dependent magnetic properties. CrystEngComm 12:373. https://doi.org/10.1039/B910550F

48. Berkowitz AE, Schuele WJ, Flanders P (1968) Influence of crystallite size on the magnetic properties of acicular γ-Fe$_2$O$_3$ particles. J Appl Phys 39:1261. https://doi.org/10.1063/1.1656256

49. Bødker F, Hansen MF, Koch CB, Lefmann K, Mørup S (2000) Magnetic properties of hematite nanoparticles. Phys Rev B 61:6826. https://doi.org/10.1103/PhysRevB.61.6826

50. Sanpo N, Berndt CC, Wen C, Wang J (2013) Transition metal-substituted cobalt ferrite nanoparticles for biomedical applications. Acta Biomater 9:5830. https://doi.org/10.1016/j.actbio.2012.10.037

51. Chia CH, Zakaria S, Yusoff M (2010) Size and crystallinity-dependent magnetic properties of CoFe$_2$O$_4$ nanocrystals. Ceram Int 36:605. https://doi.org/10.1016/j.ceramint.2009.10.001

52. Meng YY, Liu ZW, Dai HC (2012) Structure and magnetic properties of Mn (Zn)Fe$_{2-x}$RE$_x$O$_4$ ferrite nano-powders synthesized by co-precipitation and refluxing method. Powder Technol 229:270. https://doi.org/10.1016/j.powtec.2012.06.050

53. Zhang Z, Hu C, Xiong Y, Yang R, Wang ZL (2007) Synthesis of Ba-doped CeO$_2$ nanowires and their application as humidity sensors. Nanotechnology 18:465504. https://doi.org/10.1088/0957-4484/18/46/465504

54. Tasaki A, Iida S (1996) J Phys Soc Japan 16:1697

55. Amin N, Arajs S (1987) Morin temperature of annealed submicronic α-Fe$_2$O$_3$ particles. Phys Rev B 35:4810. https://doi.org/10.1103/PhysRevB.35.4810

56. Xu B, Huang B, Cheng H, Wang Z, Qin X, Zhang X, Dai Y (2012) α-Fe$_2$O$_3$ hollow structures: formation of single crystalline thin shells. Chem Commun 48:6529. https://doi.org/10.1039/C2CC33032F

57. Xue X, Hanna K, Deng N (2009) Fenton-like oxidation of Rhodamine B in the presence of two types of iron(II, III) oxide. J Hazard Mater 166:407. https://doi.org/10.1016/j.jhazmat.2008.11.089

58. Senapati KK, Borgohain C, Phukan P (2011) Synthesis of highly stable CoFe$_2$O$_4$ nanoparticles and their use as magnetically separable catalyst for Knoevenagel reaction in aqueous medium. J Mol Catal A Chem 339:24. https://doi.org/10.1016/j.molcata.2011.02.007

59. Criegee R (1972) Organic peroxides. Angew Chem Int Ed 84:905. https://doi.org/10.1002/ange.19720841823

60. Takafuji M, Ide S, Ihara H, Xu Z (2004) Preparation of poly(1-vinylimidazole)-grafted magnetic nanoparticles and their

application for removal of metal ions. Chem Mater 16:1977. https://doi.org/10.1021/cm030334y

61. Singh J, Srivastava M, Dutta J, Dutta PK (2011) Preparation and properties of hybrid monodispersed magnetic α-Fe$_2$O$_3$ based chitosan nanocomposite film for industrial and biomedical applications. Int J Biol Macromol 48:170. https://doi.org/10.1016/j.ijbiomac.2010.10.016

62. Loukanov AR, Dushkin CD, Papazova KI, Kirov AV, Abrashev MV, Adachi E (2004) Photoluminescence depending on the ZnS shell thickness of CdS/ZnS core–shell semiconductor nanoparticles. Colloids Surf A Physicochem Eng Asp 245:9. https://doi.org/10.1016/j.colsurfa.2004.06.016

63. Nikoobakht B, El-Sayed MA (2001) Evidence for bilayer assembly of cationic surfactants on the surface of gold nanorods. Langmuir 17:6368. https://doi.org/10.1021/la010530o

64. La Porta FA, Andres J, Vismara MVG, Graeff CFO, Sambrano JR, Li MS, Varela JA, Longo E (2014) Correlation between structural and electronic order–disorder effects and optical properties in ZnO nanocrystals. J Mater Chem C 2:10164. https://doi.org/10.1039/C4TC01248H

65. Tao K, Dou HJ, Sun K (2008) Interfacial coprecipitation to prepare magnetite nanoparticles: concentration and temperature dependence. Colloids Surf A Physicochem Eng Asp 320:115. https://doi.org/10.1016/j.colsurfa.2008.01.051

66. Kennedy RJ, Stampe PA (1999) Fe$_3$O$_4$ films grown by laser ablation on Si(100) and GaAs(100) substrates with and without MgO buffer layers. J Phys D Appl Phys 32:16. https://doi.org/10.1088/0022-3727/32/1/004

67. Si SF, Li CH, Wang X, Yu DP, Peng Q, Li YD (2005) Cryst Growth Des 5:391

68. Ding Y, Hu Y, Zhang LY, Chen Y, Jiang XQ (2006) Synthesis and magnetic properties of biocompatible hybrid hollow spheres. Biomacromol 7:1766. https://doi.org/10.1021/bm060085h

69. Sadykov VA, Isupova LA, Tsybulya SV (1996) Effect of mechanical activation on the real structure and reactivity of iron(III) oxide with corundum-type structure. J Solid State Chem 123:191. https://doi.org/10.1006/jssc.1996.0168

70. Rufus A, Sreeju N, Vilas V, Philip D (2017) Biosynthesis of hematite (α-Fe$_2$O$_3$) nanostructures: size effects on applications in thermal conductivity, catalysis, and antibacterial activity. J Mol Liq 242:537–549. https://doi.org/10.1016/j.molliq.2017.07.057

71. Kayani ZN, Arshad S, Riaz S, Naseem S (2014) Synthesis of iron oxide nanoparticles by sol–gel technique and their characterization. IEEE Trans Magn 50:8. https://doi.org/10.1109/TMAG.2014.2313763

72. McEvoy E, Marsh A, Altria K, Donegan S, Power J (2007) Recent advances in the development and application of microemulsion EKC. Electrophoresis 28:193. https://doi.org/10.1002/elps.200600451

73. Gharagozlou M (2011) Influence of calcination temperature on structural and magnetic properties of nanocomposites formed by Co-ferrite dispersed in sol–gel silica matrix using tetrakis (2-hydroxyethyl) orthosilicate as precursor. Chem Cent J 5. Article number 19. https://doi.org/10.1186/1752-153X-5-19

74. Pillai V, Shah DO (1996) Synthesis of high-coercivity cobalt ferrite particles using water-in-oil microemulsions. J Magn Magn Mater 163:243. https://doi.org/10.1016/S0304-8853(96)00280-6

75. Theyvaraju D, Muthukumaran S (2015) Preparation, structural, photoluminescence and magnetic studies of Cu doped ZnO nanoparticles co-doped with Ni by sol–gel method. Phys E Low Dimens Syst Nanostruct 74:93. https://doi.org/10.1016/j.physe.2015.06.012

76. Kumar S, Chen CL, Dong CL, Ho YK, Lee JF, Chan TS, Thangavel R, Chen TK, Mok BH, Rao SM, Wu MK (2013) Room temperature ferromagnetism in Ni doped ZnS nanoparticles. J Alloys Compd 554:357. https://doi.org/10.1016/j.jallcom.2012.12.001

77. Krishnakanth R, Jayakumar G, Albert Irudayaraj A, Dhayal Raj A (2016) Structural and magnetic properties of NiO and Fe-doped NiO nanoparticles synthesized by chemical co-precipitation. Method Mater Today Proc 3:1370. https://doi.org/10.1016/j.matpr.2016.04.017